Materials Characterization 182 (2021) 111552

Contents lists available at ScienceDirect

Materials Characterization

journal homepage: www.elsevier.com/locate/matchar

Examining the pathways for deformation band formation at the mesoscale

John Rotella [a,b], Adam L. Pilchak [b,c], Michael D. Sangid [a,d,*]

[a] School of Materials Engineering, Purdue University, 701 W. Stadium Ave., West Lafayette, IN 47907, USA
[b] Air Force Research Lab, AFRL/RXCM, Wright Patterson AFB, OH 45433, USA
[c] Materials Resources LLC, 2650 Indian Ripple Road, Dayton, OH 45344, USA
[d] School of Aeronautics and Astronautics, Purdue University, 701 W. Stadium Ave., West Lafayette, IN 47907, USA

ARTICLE INFO

Keywords:
Titanium alloys
Grain boundaries
Deformation pathways
Representative volume element
Tension-torsion loading

ABSTRACT

At the macroscopic scale, strain accumulation is known to form parallel to the plane of maximum shear stress. In this work, plastic strain accumulation is tracked across four mesoscale areas of interests. Each representing a different configuration of tension-torsion loading. The local deviations in the deformation pathways were investigated relative to the plane of maximum shear stress. The deviations in the deformation pathways were observed to be a function of the local plastic strain magnitude and the microstructural features. From these results, a representative volume element was created based on the macroscopic and micromechanical deformations as well as the spatial statistics of the deformation bands.

1. Introduction

The development of the deformation pathways within polycrystalline materials is a multi-scale process, wherein the macroscopic loading conditions and local microstructure dictate the mechanical response [1,2]. At the nanoscale, plastic deformation manifests as arrays of dislocations, i.e., slip bands within the material. Dislocations progress to grain boundaries (GBs) wherein they experience cross-slip, direct transmission, indirect transmission or no transmission [3]. Deformation bands, DBs, are created when slip events become inter-connected through many grains within the microstructure.

At the macroscopic scale, the primary pathways of deformation occur in the plane of maximum shear stress (MSS) [4] as determined by the loading condition and calculated through a Mohr's circle analysis [5–7]. These deformation pathways consist of both crystallographic and non-crystallographic deformation based on the local strain magnitudes [6,7]. In many cases, a slip plane is not directly aligned with the plane of MSS, and thus slip events across neighboring grains may be required, such that their cumulative deformation corresponds to the plane of MSS [8,9].

At the microstructural scale, the largest degree of deformation is observed to localize near the GBs [10]. Compatibility constraints and dislocation motion increase stress and promote deformation near GBs. Compatibility stresses are caused by neighboring grains with different crystallographic orientations, and localized deformations in adjacent grains [11]. Additional stresses are experienced due to dislocation pile-ups at a GB [12]. These complex stresses are relieved through slip transmission or the activation of an adjacent slip system. These slip events create a network of inter-connected slip events, which have shown to be key features in crack initiation and material failure [13,14]. Due to the consequences of localized deformation at GBs, spatially resolved deformation tracking methods have been developed.

Previous studies have implemented techniques such as digital image correlation (DIC) [15], electron back scatter diffraction (EBSD) [16] or combinations of both techniques [10] to study deformation across length scales. The single camera DIC technique tracks the in-plane displacement of features, often referred to as a speckle pattern, on a surface between a reference state and deformed state. The resolution is enhanced by utilizing a speckle pattern that is fine, random and dense [17] relative to the microstructural features of interest, such as grain size [18]. In uniaxial deformation, DIC studies have observed partitioning of strain accumulation into banded structures which form parallel to the plane of MSS [10,19]. These banded structures are synonymous with the aforementioned DBs. Lunt et al. [20] quantified the in-plane strain partitioning of the DB features, wherein the DBs accumulated up to four times the amount of strain as compared to regions without these features.

In addition to GBs, other microstructural features such as grain size [13,21–23] and crystallographic texture [24–29] are important factors influencing the local deformation behavior. Hall [21] and Petch [22]

* Corresponding author at: Purdue University, 701 W. Stadium Ave., West Lafayette, IN 47907, USA.
E-mail address: msangid@purdue.edu (M.D. Sangid).

https://doi.org/10.1016/j.matchar.2021.111552
Received 30 July 2021; Received in revised form 21 September 2021; Accepted 23 October 2021
Available online 27 October 2021

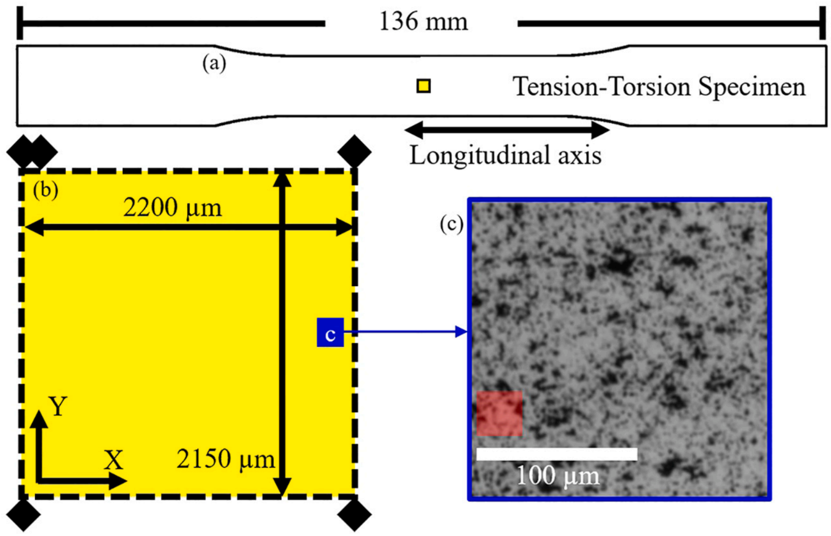

Fig. 1. (a) A scale representation of the tension-torsion specimen displaying the position and size of the AOI. (b) The dimensions of the AOI for each specimen, with specified subregion of interest. (c) Subregion of interest, displaying titanium nanoparticle speckle pattern. The translucent red box represents the subset size utilized for the DIC analysis, 28 μm. (For interpretation of the references to color in this figure legend, the reader is referred to the web version of this article.)

observed that material strength was inversely proportional to grain size. Deformation in smaller grains is more difficult due to the shorter mean free path between dislocations and GBs. As a consequence of dislocation pile-up, back stresses are imposed on the primary slip systems which cause secondary slip activity and work hardening [30]. In titanium alloys, a grain is termed "hard" or soft" based on the c-axis orientation relative to the loading axis, where a hard grain has a c-axis that is near parallel to the loading direction. Conversely, soft grains have a c-axis that is nearly perpendicular to the loading direction and are well oriented for basal slip and prismatic slip. At the bulk scale, Evans et al. [29] observed crack initiation of textured materials is controlled by the basal planes orientation relative to the plane of MSS, where better alignment resulted in shorter material life. At the microscale, Harr et al. [28] observed grains well oriented for basal slip create long range slip traces which can traverse over 100 grain diameters.

Polycrystalline deformation models address many length scales of deformation phenomena by simulating explicit or representative deformation behavior. A representative volume element (RVE), is the minimum volume simulated that captures the ensemble mechanical behavior and was described by Hill [31]. The characteristics of a RVE were described in two parts where (i) the distribution and dispersion of the microstructural features are matched to the material simulated and (ii) the volume is large enough such that the effective properties are independent of the boundary effects. In accordance with Hill's description, RVEs are commonly sized by matching a set of microstructural descriptor distributions [32], such as grain size, texture, grain morphology, etc. Additional verification for RVEs may include matching various mechanical properties, such as yield strength and hardening rate [33]. In addition to the two common methodologies above, RVE sizing interpretation has also been investigated by matching the spatial variability of in-plane plastic strain [34] or grain-to-grain variability based on elastic strains [35]. Balzani et al. [36] proposed a methodology to size an RVE, which minimized the error in the overall macroscopic deformation response while also considering the distribution of microstructural features within the RVE. This approach differs from the aforementioned approaches because it utilizes the post experimental deformation behavior at two length scales and does not consider any of the typical microstructural descriptors. Lastly, two-point statistics (autocorrelation and, cord length distributions) are commonly utilized to characterize the spatial occurrence of features such as c-axis orientation [37] and microtextured zones [38]. However, it is noted that these two-point functions capture the average behavior and thus they should be utilized with additional characterization methods for improved accuracy of the RVE construction.

In this work, the deformation occurring parallel to the plane of MSS is decoupled from the microstructure-based strain accumulation via a series of multiaxial tension-torsion experiments, which vary the plane of MSS. By removing the effect of the plane of MSS, the influence of microstructural features, such as grain size, grain orientation and GBs, on the developing primary and secondary deformation pathways can be assessed over many grains. Where the primary deformation pathways are aligned with the plane of MSS, and the secondary deformation pathways are any deviations from the plane of MSS. Given the discrepancy between these deformation length scales, millimeters of material are interrogated. Deviations within DBs are correlated by their distance from the GBs and degree of plastic strain accommodation to investigate the role of microstructural features on the development of deformation pathways. Four separate stress states, torsion, tension, 2:1 tension and 2:1 torsion, were characterized via DIC and EBSD. The orientation of the DBs were characterized via two-point statistics and compared against the plane of MSS. The trends reported here are consistent for each of the global stress states. Finally, the characterized DB measurements, macroscopic residual strain, $E_{Total}^{residual}$, and micromechanical fields are utilized to inform a RVE size, which is compared against prior RVE instantiations on similar and engineering variations of the material.

2. Materials and methods

2.1. Material pedigree and specimen preparation

The material system studied in this experiment was a near alpha phase titanium alloy, Ti-7Al, with a hexagonal closed packed crystal structure. The Ti-7Al material was cast into ingot form, hot isostatic

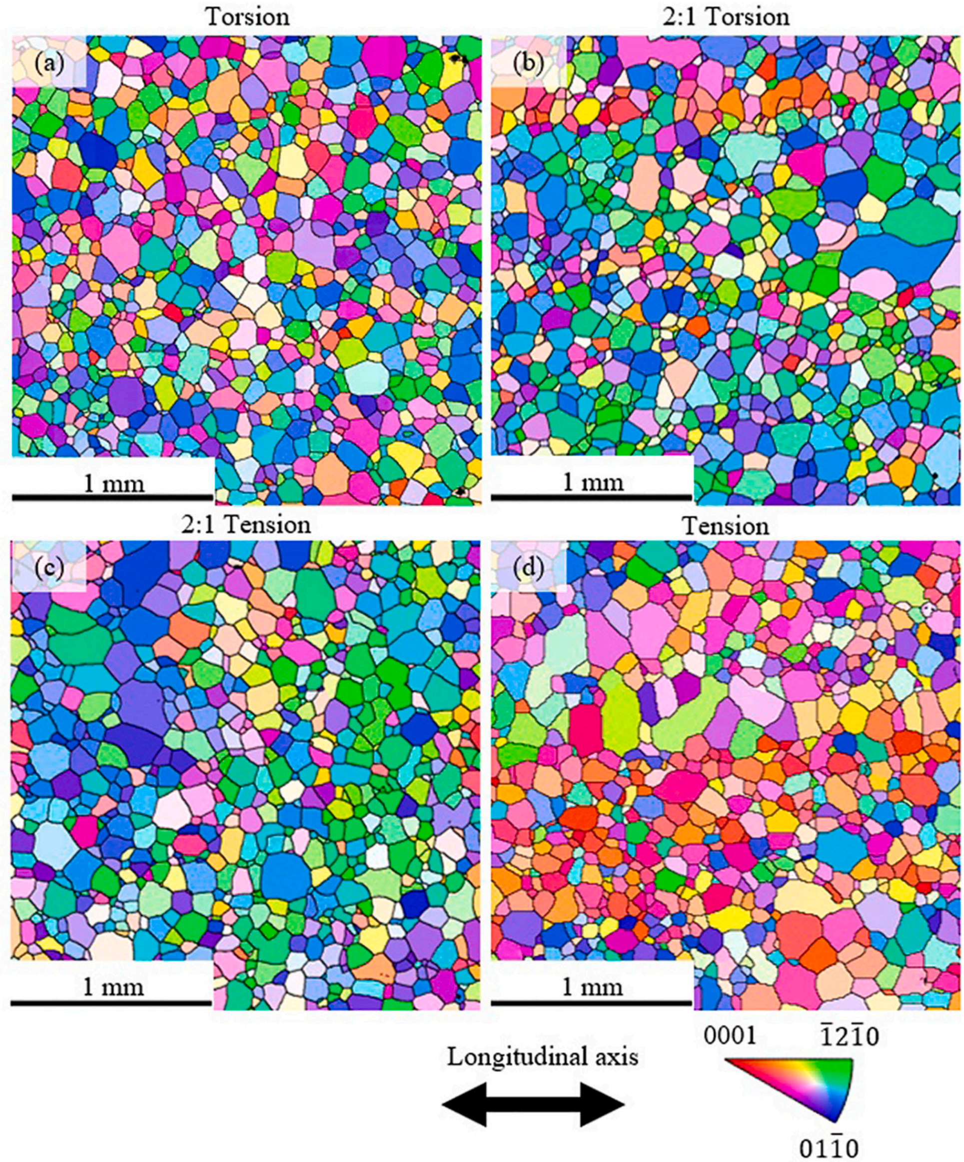

Fig. 2. The normal-direction inverse pole figure representations for each of the analyzed AOIs are shown for the macroscopic loading states; (a) torsion, (b) 2:1 torsion, (c) 2:1 tension and (d) tension specimens. The longitudinal axis is denoted for all specimens.

Table 1
The peak tensile strain ($E_{Applied}^{Tension}$) and shear strain ($\Gamma_{Applied}^{Shear}$) applied macroscopically to each specimen. The residual macroscopic strain of each specimen, $E_{Total}^{residual}$.

	$E_{Applied}^{Tension}$	$\Gamma_{Applied}^{Shear}$	$E_{Total}^{residual}$	$\bar{\gamma}^{max}$
Torsion	0	0.006	0.002	0.002
2:1 torsion	0.003	0.005	0.0008	0.003
2:1 tension	0.005	0.003	0.0008	0.004
Tension	0.006	0	0.0005	0.006

The average maximum in-plane shear strain within each specimen's AOI, $\bar{\gamma}^{max}$.

Table 2
The tensile ($\dot{\varepsilon}_{Tensile}$), shear ($\dot{\varepsilon}_{Shear}$), and combined ($\dot{\varepsilon}_{Combined}$) strain rates ($s^{-1}$) for each loading condition.

Loading condition	$\dot{\varepsilon}_{Tensile}$ (s^{-1})	$\dot{\varepsilon}_{Shear}$ (s^{-1})	$\dot{\varepsilon}_{Combined}$ (s^{-1})
Torsion	–	6.80E-05	6.80E-05
2:1 tension	3.40E-05	1.75E-05	3.81E-05
2:1torsion	1.67E-05	3.17E-05	3.58E-05
Tension	3.35E-05	–	3.35E-05

pressed, extruded and annealed at 955 °C for 24 hours, followed by an air cool [39]. The resulting material contained equiaxed grains with an average grain size of 86 μm. In order to create specimens, gauge sections of Ti-7Al were extracted and friction stir welded to circular gripping end pieces of Ti-6 V-4Al. A 10 mm, square-cross section, gauge length was machined from the Ti-7Al portion to complete the specimen geometry, as shown in Fig. 1a. Each specimen was machined and electro-polished to create a mirror finish, enabling spatial orientation characterization via EBSD.

An area of interest (AOI) measuring 2150 μm by 2250 μm was

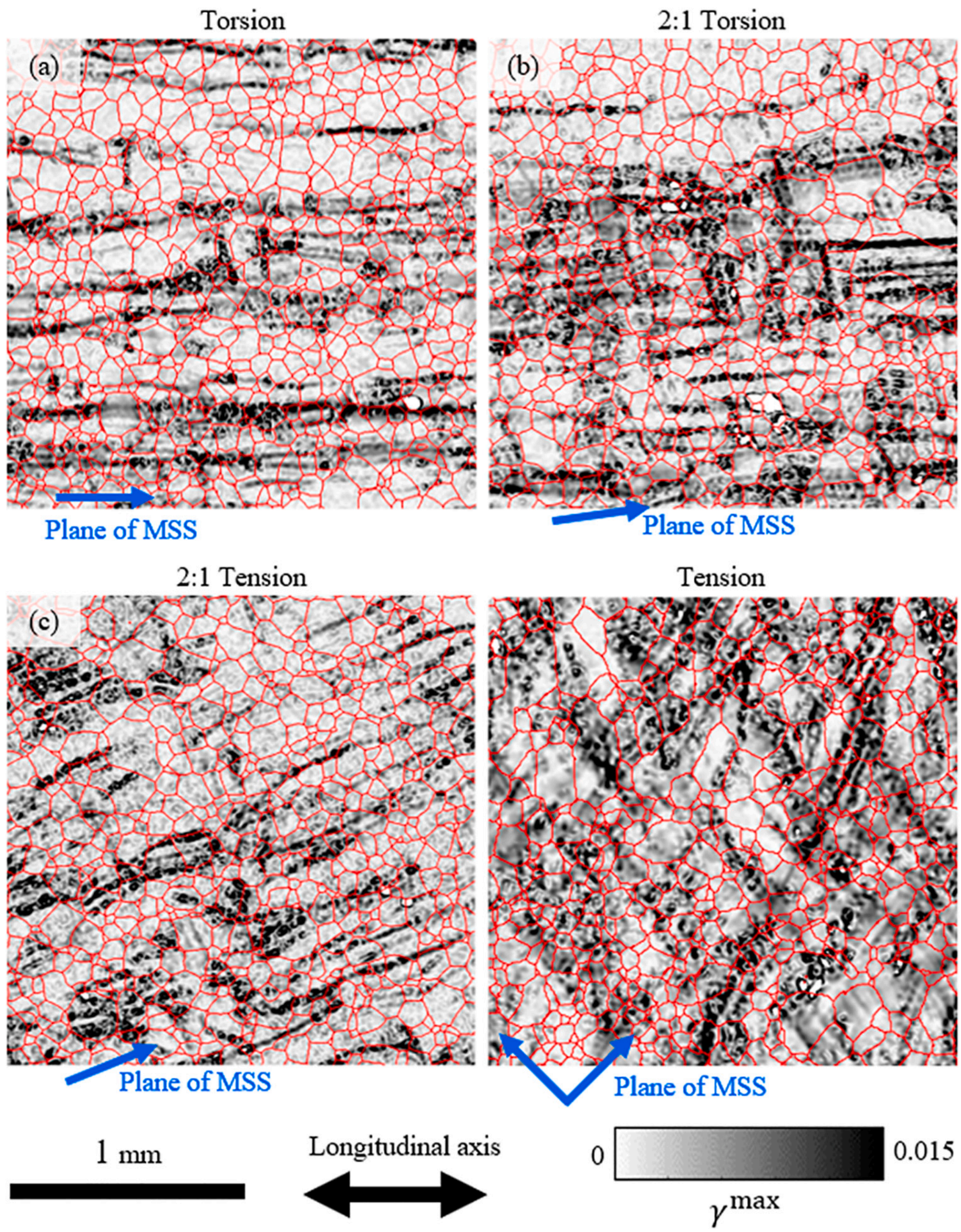

Fig. 3. Strain maps displaying the γ^{max}, for the (a) torsion, (b) 2:1 torsion, (c) 2:1 tension and (d) tension specimens. The plane of MSS is delineated by an arrow for each specimen.

marked within the gauge section using Vickers indents as fiducial markers, which were placed using a LECO Microhardness Tester, model LM247AT. The fiducial marker pattern is shown in Fig. 1b. The fiducial markers served a two-fold purpose; (i) establish an AOI and (ii) provide spatial reference markings to consolidate the DIC and EBSD datasets. Crystallographic orientation data was collected via EBSD utilizing an Oxford symmetry detector, with a step size of 2 μm. The GBs were defined by a 5° misorientation tolerance. The normal-direction inverse pole figure maps for each specimen are shown in Fig. 2.

2.2. Experimental details

Four tension-torsion experiments were conducted in an MTS Model 809 servo hydraulic test system with a MTS biaxial extensometer, model 632, to monitor the applied tensile and shear strains. Each specimen was loaded in stress control to the same target least squares strain, E_{Total}, of 0.006 as defined by Eq. 1, wherein $E_{Applied}{}^{Tension}$ and $\Gamma_{Applied}{}^{Shear}$ are the applied tensile strain and shear strain applied to the specimen, respectively.

$$E_{Total} = \sqrt{E_{Applied}^{Tension\,2} + \Gamma_{Applied}^{Shear\;\;2}} \tag{1}$$

The E_{Total}, 0.006, value was chosen such that the applied load would be just beyond the yield stress of the material. The choice in the E_{Total} ensured sufficient deformation was imparted to make DB identification possible and avoided difficulties that may have resulted by large deformations, such as uniquely distinguishing DBs or damage to the DIC speckle pattern. Specimens were returned to zero shear strain, to ensure

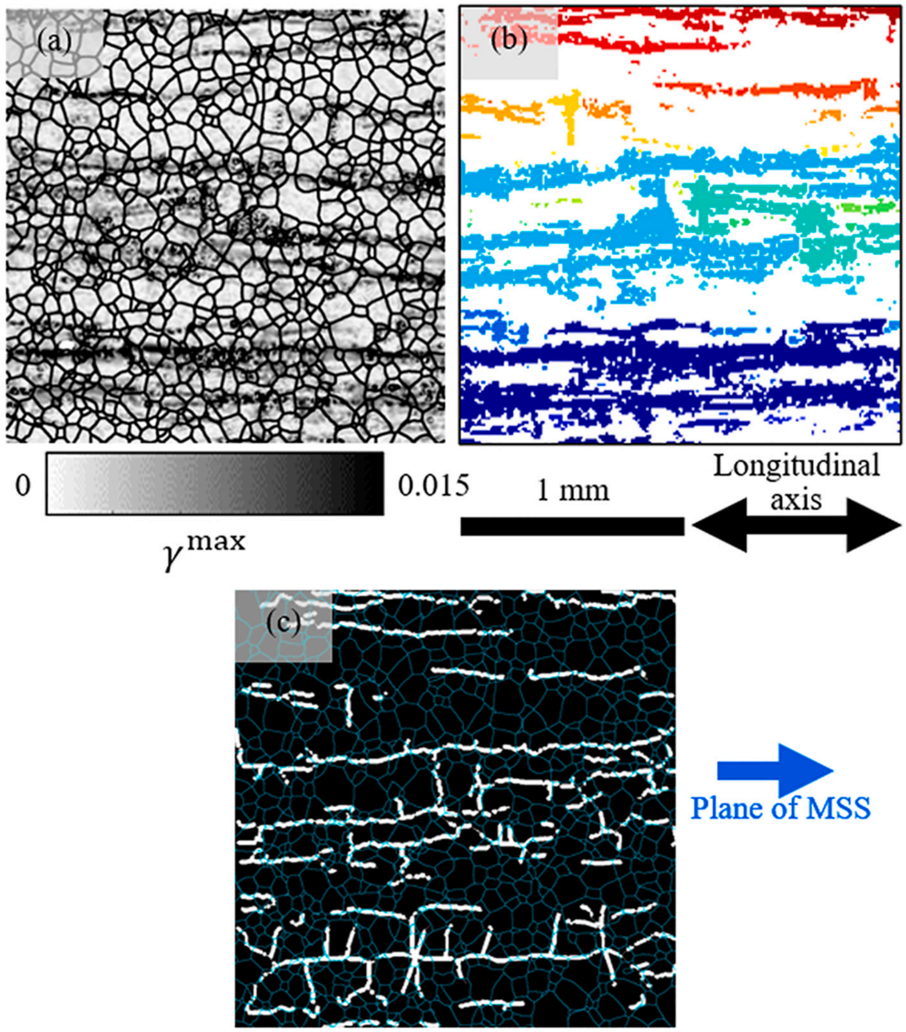

Fig. 4. (a) Strain map displaying the γ^{max} of the torsion specimen. (b) DBs are identified by unique colors following the percolation strain at 0.003. (c) A skeletonized representation of each DB represented in (b). GBs are represented by black and teal lines in (a) and (c), respectively. The longitudinal axis and plane of MSS are delineated by arrows. (For interpretation of the references to colour in this figure legend, the reader is referred to the web version of this article.)

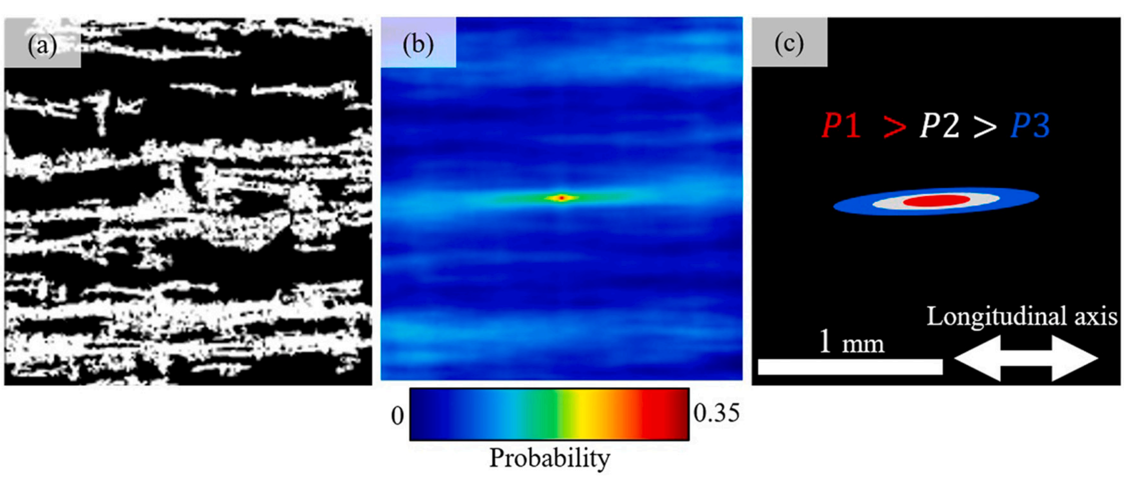

Fig. 5. (a) Binary DB map for the torsion specimen. (b) Self-correlation of image (a). (c) Iso-probability contours as traced by ellipsoid fitting, wherein each ellipse represents a different probability contour. Note that a larger probability value such as P1 corresponds to a fit ellipse with smaller area.

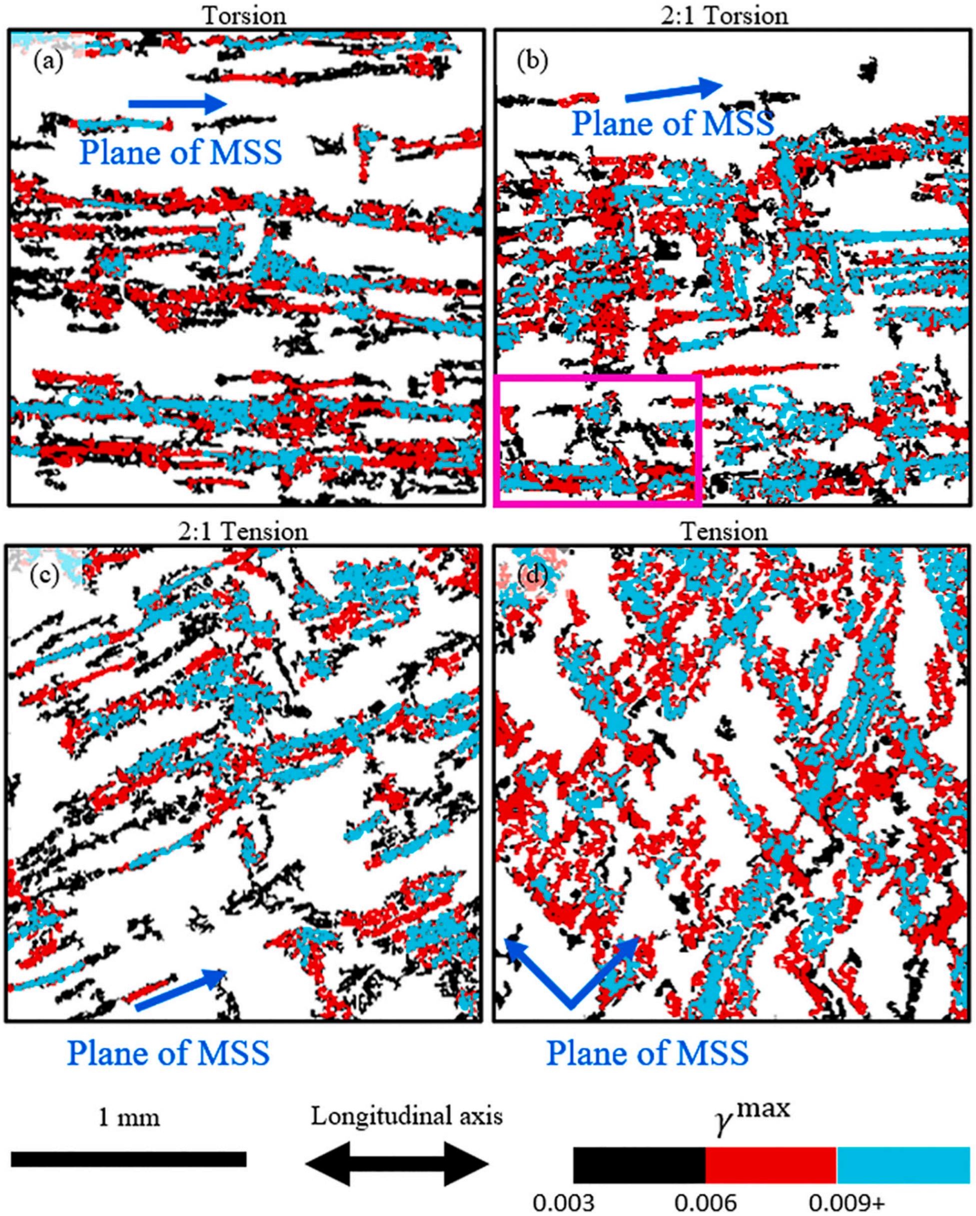

Fig. 6. DBs are shown at multiple percolation strains, 0.003, 0.006 and 0.009, for the loading conditions: (a) torsion, (b) 2:1 torsion, (c) 2:1 tension and (d) tension specimens. The theoretical angle of the deformation, the plane of MSS, is annotated for each loading condition. The box region in (b) will be discussed in Fig. 8.

Table 3
The range of DB inclination angles from autocorrelation and the angle of the plane of MSS, relative to the longitudinal axis of the specimen.

	Inclination angle	
	Range from autocorrelation	Plane of MSS
Torsion	0° - 5°	0°
2:1 torsion	3° - 10°	7.88°
2:1 tension	19° - 27°	22.5°
Tension	41° - 44°	45°

a near planar surface for the DIC technique, and zero tensile load, before being removed from the load frame. Therefore, the residual macroscopic strain, $E_{Total}^{residual}$ for each specimen is different, where the $E_{Total}^{residual}$ is proportional to the applied shear strain. Tension-torsion experiments of varying ratios were conducted on 4 specimens, the specific experimental conditions were torsion, tension, 2:1 tension and 2:1 torsion. Where the ratio 2:1, indicates the fraction of the applied strains. The applied strain conditions and residual strain for each specimen are shown in Table 1 within columns 1, 2 and 3.

The tensile strain rate ($\dot{\varepsilon}_{Tensile}$), shear strain rate ($\dot{\varepsilon}_{Shear}$) and combined strain rate ($\dot{\varepsilon}_{Combined}$) for each specimen were on the order of 1E^{-5} s^{-1} and are listed within Table 2 for each loading condition. The combined strain rate was determined by substituting strain rate for strain within Eq. 1.

2.3. Digital image correlation

Titanium nanoparticles, with a mean size of 80 nm, were applied to

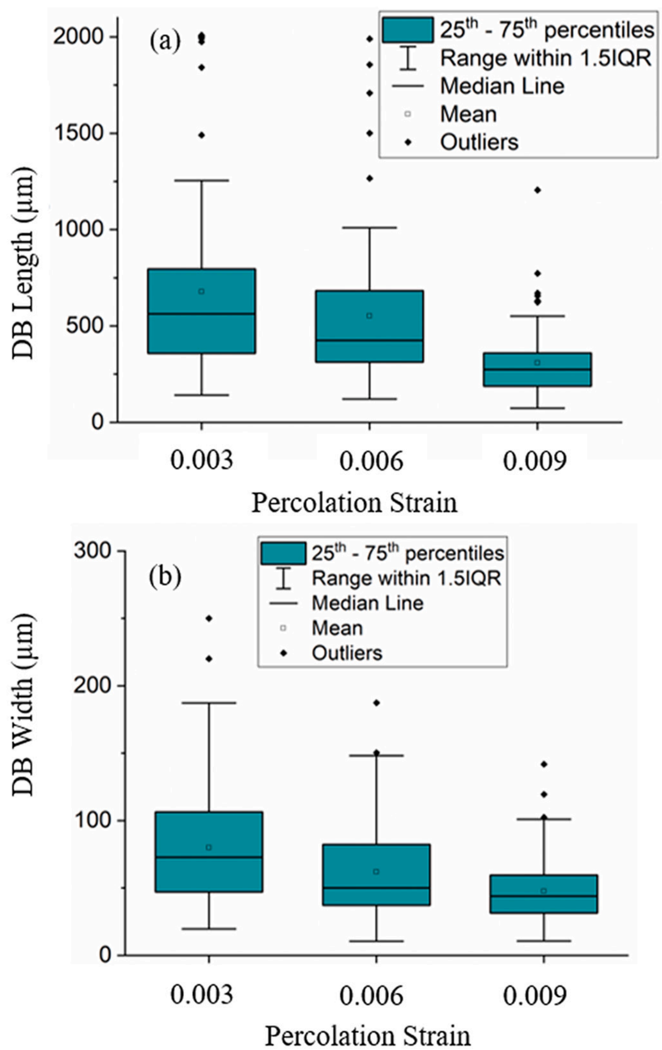

Fig. 7. Deformation band measurements of the (a) length and (b) thickness at percolation strains 0.003, 0.006 and 0.009.

each specimen to enable DIC following specimen deformation, as shown in Fig. 1c. The nano-particle solution was prepared and applied in accordance with Tracy et al. [40]. A Zeiss Axio Imager with a total magnification of 50x was utilized to capture images at a resolution of 1960 × 1460 pixels or 0.9 $\frac{\mu m}{pixel}$. In total, four images with 15% overlap were needed to capture each AOI. DIC was performed with the Correlated Solutions VIC2D software package utilizing a subset of 28 μm and a step size of 1.8 μm, as shown in Fig. 1c.

Full field deformation was captured utilizing the DIC technique and overlaid with the microstructure as captured via EBSD. To account for all in-plane strains captured within the dataset, the maximum in-plane shear strain, γ^{max}, was calculated for each spatial point utilizing Eq. 2 [41], wherein ε_{xx}, ε_{yy}, and ε_{xy} are the axial, transverse, and in-plane shear strains at each pixel location, respectively.

$$\gamma^{max} = \sqrt{\left(\frac{\varepsilon_{xx} - \varepsilon_{yy}}{2}\right)^2 + \left(\frac{\varepsilon_{xy}}{2}\right)^2} \tag{2}$$

The resulting γ^{max} maps for each specimen are shown in Fig. 3. Regions of localized plastic strain present as discrete bands within the microstructure and are observed to form at varying angles based on the imposed stress state. The plane of MSS for each loading case is superimposed. The average maximum in-plane shear strain, $\overline{\gamma}^{max}$, for each specimen's AOI is shown in column 4 of Table 1.

2.4. Deformation band identification and orientation analysis

DBs were identified by utilizing a series of applied strain thresholds and applying percolation theory as series of a fill-flood actions. By utilizing this method of segmentation, a DB can be described as the interconnectivity of the plastic deformation resulting from the imposed macroscopic deformation [42]. The results of this analysis will be referred to as the percolation strain throughout the article. First, a strain threshold and MATLAB based percolation algorithm [43] are applied to the original γ^{max} maps, as shown in Fig. 4a. The percolation algorithm utilized strain thresholds as high pass filters and subsequently fill-flood commands to identify and cluster 8-connected pixels [43] with γ^{max} magnitudes above 0.003, 0.006 and 0.009. Each cluster is defined as a DB and is shown as a unique color for the torsion specimen in Fig. 4b. Each DB was skeletonized, allowing for each spatial point within the DB to be referenced to other microstructural features such as GBs, as shown in Fig. 4c.

An autocorrelation [44,45] was utilized to establish the mean orientation of the DBs within each specimen. The autocorrelation utilized binarized data, where the DBs are represented by white and the surrounding matrix is black, as shown in Fig. 5a. The autocorrelation produced a spatial probability map which corresponds to the likelihood of the DBs overlapping one another, as shown for the torsion specimen in Fig. 5b. Iso-probabilities were represented by ellipses fit to the autocorrelation probability map as shown schematically in Fig. 5c, wherein the greatest and lowest iso-probability contour correspond to P1 and P3, respectively. The mean orientation of DBs or inclination angle within each specimen was defined as the angle between the major axis of the fit ellipse and the longitudinal axis. The range of isoprobability values were consistent for each percolation strain and were selected via inspection to allow ellipse fitting over the largest range of probability values.

2.5. RVE construction via a combination of the macroscopic and micromechanical deformation response

The following procedure establishes a mesoscale RVE edge length that satisfies the macroscopic and micromechanical strain state of the material. The following methodology has been modified to utilize plastic strain data from the original methodology presented by Balzani et al. [36], who utilized stresses obtained through finite element simulations. The procedure first establishes an area which minimizes the error between the $E_{Total}^{residual}$ and the $\overline{\gamma}^{max}$ of a potential RVE window, which varies in size. The edge length of the window with be referred to as the RVE edge length. The micromechanical analysis informs the number of DBs features which will fit within the established mesoscale RVE by matching feature statistics throughout the AOI. The RVE model established by these methods will be referred to as the mesoscale plastic strain sizing (MPSS) model.

2.5.1. Macroscopic RVE sizing approach

The macroscopic approach utilizes a minimization of a least squares functional to determine the RVE edge length which minimizes the overall deformation response error, relative to the $E_{Total}^{residual}$. First, the reasonable deviation, r, is computed for each specimen and for each RVE edge length that fits within the AOI. The value r is derived by normalizing the difference between the $E_{Total}^{residual}$ and the average maximum

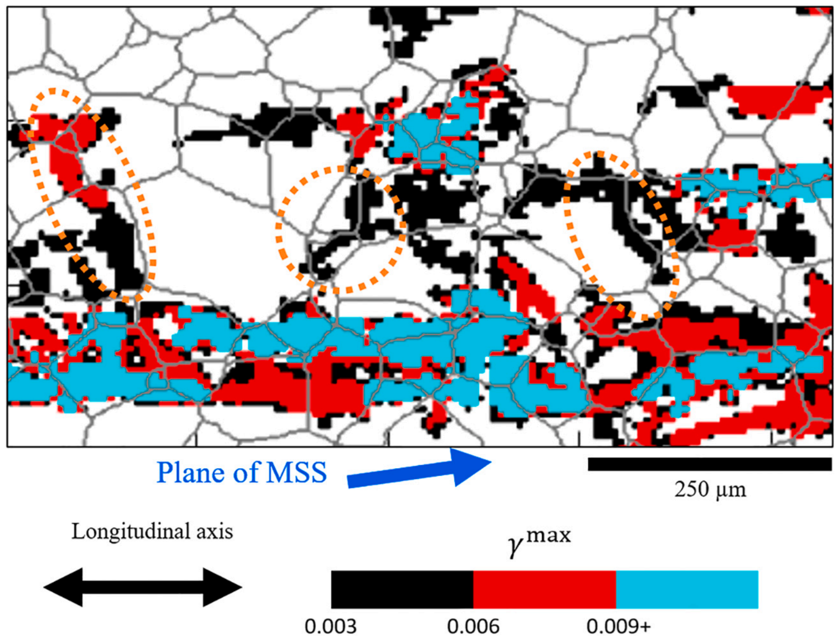

Fig. 8. DBs with superimposed GBs of a subsection of the 2:1 torsion AOI, at three percolation strains, 0.003, 0.006 and 0.009. Specific instances of deformation deviations near GBs at a percolation strain of 0.003 are encircled. DBs with magnitudes of 0.009 or larger are observed to form nearly parallel to the plane of MSS.

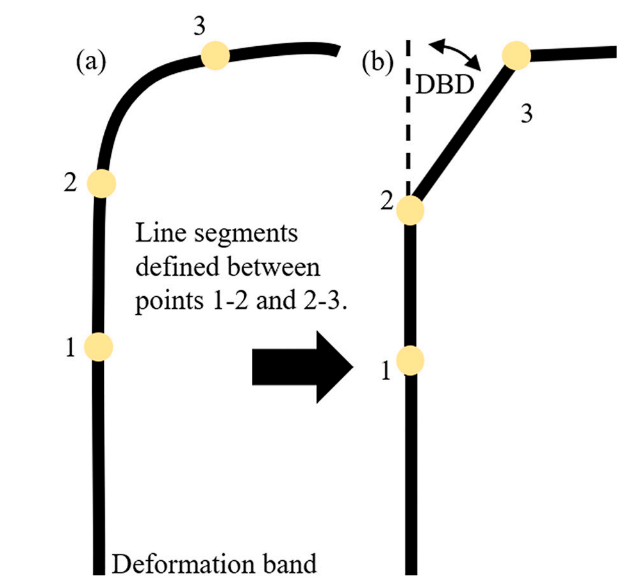

Fig. 9. (a) A deformation band is shown in segments, where each segment begins or terminates at a circle. (b) The deformation band deflection, DBD, is shown schematically between points 1–2 and points 2–3.

in-plane shear strain within that specific RVE, $\overline{\gamma}_{RVE}^{max}$, as described by Eq. 3.

$$r = \frac{E_{Total}^{residual} - \overline{\gamma}_{RVE}^{max}}{E_{Total}^{residual}} \tag{3}$$

The average macroscopic error, $\widetilde{r}$, is then computed separately for each specimen utilizing the list of r values for each RVE edge length and is defined as

$$\widetilde{r} = \sqrt{\frac{1}{n_{ep}}\sum\nolimits_{j=1}^{n_{ep}}\left(r_j^2\right)} \tag{4}$$

where n_{ep} is the number of RVE edge lengths over which r was calculated. The overall mechanical error, $r_{\widetilde{\varnothing}}$, incorporates $\widetilde{r}$ of all specimens into a single value per RVE edge length and is defined as.

$$r_{\widetilde{\varnothing}} = \sqrt{\frac{1}{n_{exp}}\sum\nolimits_{j=1}^{n_{exp}}\widetilde{r}^2} \tag{5}$$

where n_{exp} is the number of experiments (i.e., specimens). The $r_{\widetilde{\varnothing}}$ is determined for all RVE edge lengths and decreases exponentially with increasing RVE edge length. Therefore, the RVE edge length which minimizes the $r_{\widetilde{\varnothing}}$ over all loading cases can be determined.

2.5.2. Micromechanical RVE sizing approach

The micromechanical methodology quantifies the number of microstructural features that should statistically occur within the RVE previously sized by the macroscopic approach. The DB area fraction, DB_{AF}, was utilized to approximate the micromechanical variability throughout the AOIs and is defined as.

$$DB_{AF} = \frac{Pixel_{DB}}{Pixel_{AOI}} \tag{6}$$

where the number of pixels occupied by DBs and the total number of pixels within the AOI are defined as $Pixel_{DB}$ and $Pixel_{AOI}$, respectively. The average DB area fraction, $\overline{DB}_{AF}$, was utilized to compute the number of DBs, n_{DB}, per RVE edge length as shown in Eq. 7.

$$\text{RVE edge length} = \sqrt{\frac{n_{DB}\overline{A}_{DB}}{\overline{DB}_{AF}}} \tag{7}$$

Where the $\overline{A}_{DB}$ is the average area of a DB for each specimen and was calculated by utilizing the mean thickness and mean length of the DBs at

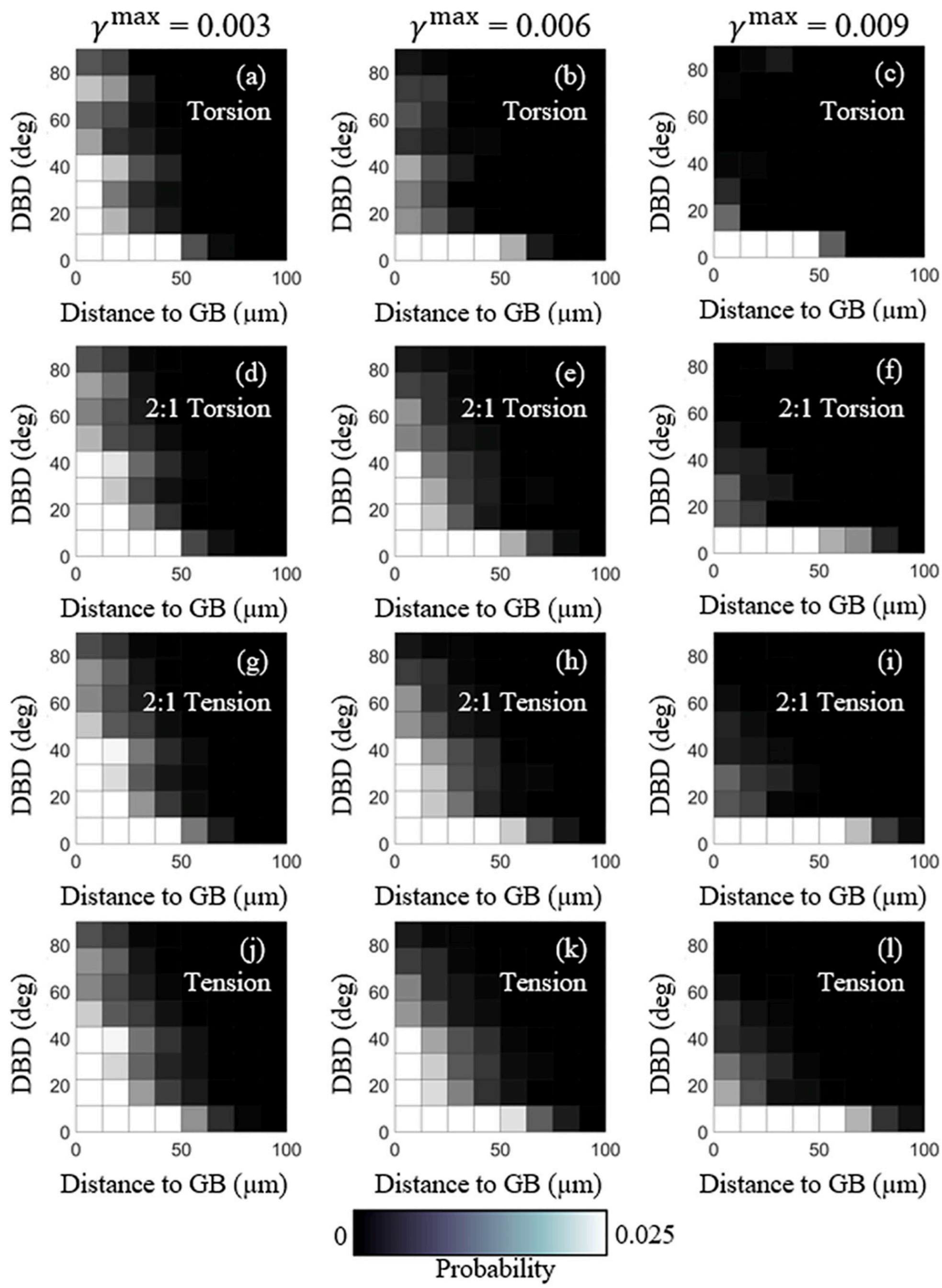

Fig. 10. The deformation band deviation, DBD, as a function of distance to the nearest GB, and percolation strain values. γ^{max} of 0.003 (left column), 0.006 (center column) and 0.009 (right column) are shown for loading states (a – c) torsion, (d – f) 2:1 torsion, (g – i) 2:1 tension, and (j – l) tension.

each percolation strain. The n_{DB} is the only unknown and is solved for by utilizing the RVE edge length previously established in Section 2.5.1.

3. Results

The principle results of this study are three-fold, (i) the DB descriptors of orientation, length and width are characterized at three percolation strains, (ii) the preference for DB formation and perturbation throughout the microstructure are investigated relative to three percolation strains and microstructural features, and (iii) a mesoscopic RVE size that satisfies both the macroscopic deformation state as well as matches the micromechanical variability along microstructural features is identified utilizing the aforementioned methodologies.

3.1. The macroscopic orientation and morphology of deformation bands

The degree of strain accumulation within the deformation pathways were examined for each loading case. The plastic strain was binned

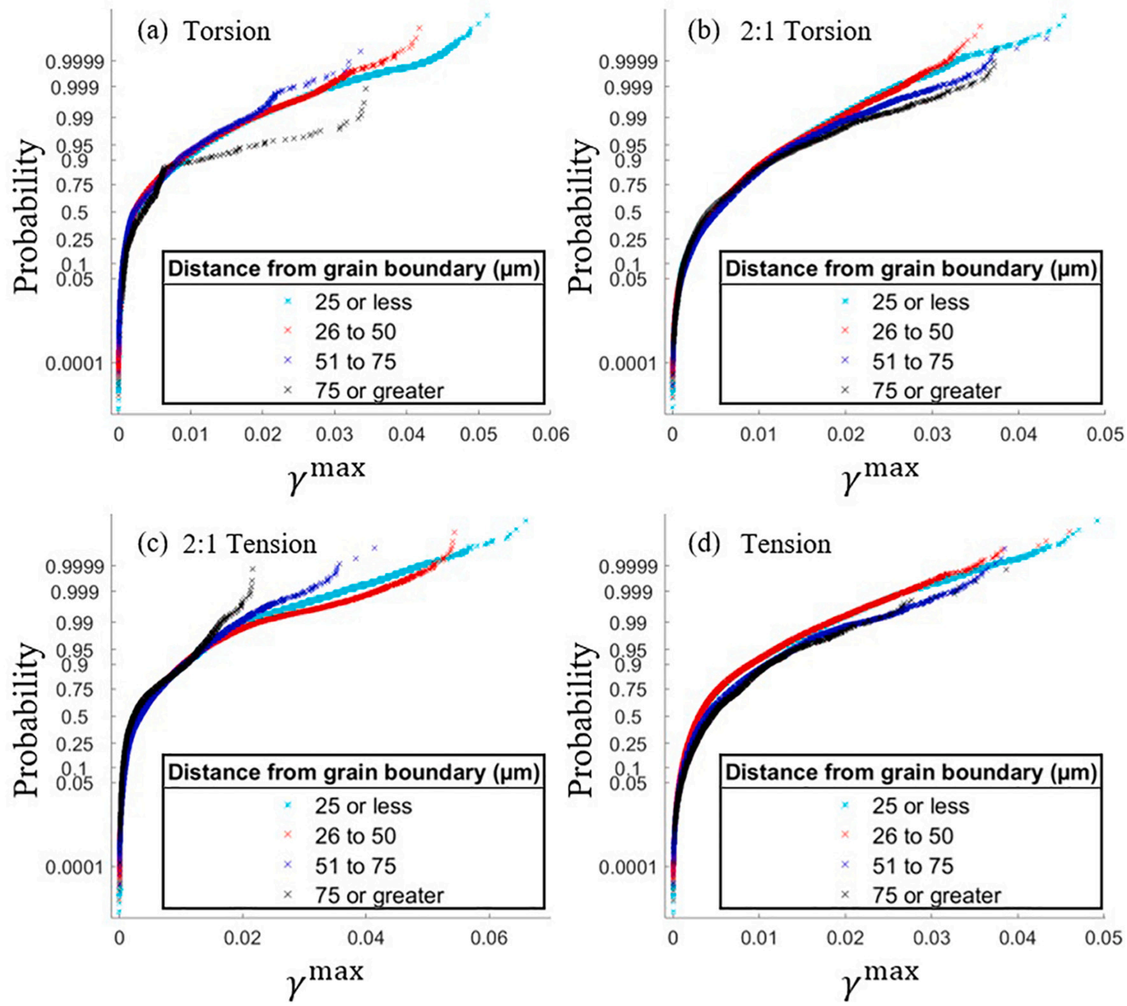

Fig. 11. The distribution of γ^{max} as a function of the distance to the nearest GB, as shown for the (a) torsion, (b) 2:1 torsion, (c) 2:1 tension and (d) tension specimens.

utilizing percolation strains of 0.003, 0.006 and 0.009, as shown for all specimens in Fig. 6. For each loading configuration, the plane of MSS is superimposed on each γ^{max} map. In general, the greatest strain accumulations occur parallel to the plane of MSS and begin to deviate from the plane of MSS as the percolation strain is decreased. A region in Fig. 6b has been boxed for subsequent interpretation.

The mean orientation of all DBs within each specimen were examined utilizing the autocorrelation method previously described in Section 2.4. The range of DB inclination angles and the plane of MSS for each loading case, relative to the longitudinal axis, are shown in Table 3. The DB inclination angles from the autocorrelation technique were near the expected deformation angles. DBs were observed to form within 5° of the planes of MSS.

The length and thickness of each DB was quantified utilizing ImageJ [46] for all percolation strains. The length of a DB was defined as the Euclidean distance from end-to-end. Along each DB, the width was measured approximately every 100 μm. The DB measurements for all percolation strains are shown in Fig. 7. All presented statistical descriptors of the length and width of the DBs were inversely proportional to the percolation strain. A few DBs spanned the entire AOI, thus the mean lengths may be larger than classified. The maximum width of a DB was approximately 3 grain diameter or 250 μm.

3.2. The effect of grain boundaries on the pathway of deformation bands

The pathways of deformation were examined relative to GBs and based on the degree of accommodated strain. A visual inspection of the DBs relative to GBs, was conducted, a representative region is shown in Fig. 8. Fig. 8 was created by superimposing the GBs onto the DBs previously shown in the boxed region of Fig. 6b. As expected, the plastic deformation accumulated parallel to the plane of MSS. However, several encircled regions show deformation which deviated from the plane of MSS near GBs. These deviations appeared more common at lower percolation strains and are investigated further in the following analysis.

The ability of a GB to influence the pathway of DBs was examined by characterizing the angular deviation of each DB relative to the nearest GB at each percolation strain. First, a skeletonized DB was divided into segments measuring 16 μm in length, as shown in Fig. 9a. Note, this analysis has been repeated with DB segments ranging between 8 μm and 20 μm in length with no effect on the reported trends. Next, the angle between adjacent DB segments was determined. This quantity is defined as the deformation band deviation (DBD), as shown within Fig. 9b. Once a DBD was determined for a DB segment, all pixels within that DB segment would be assigned that DBD. The distance between DB segments and the nearest GB was determined by measuring the distance

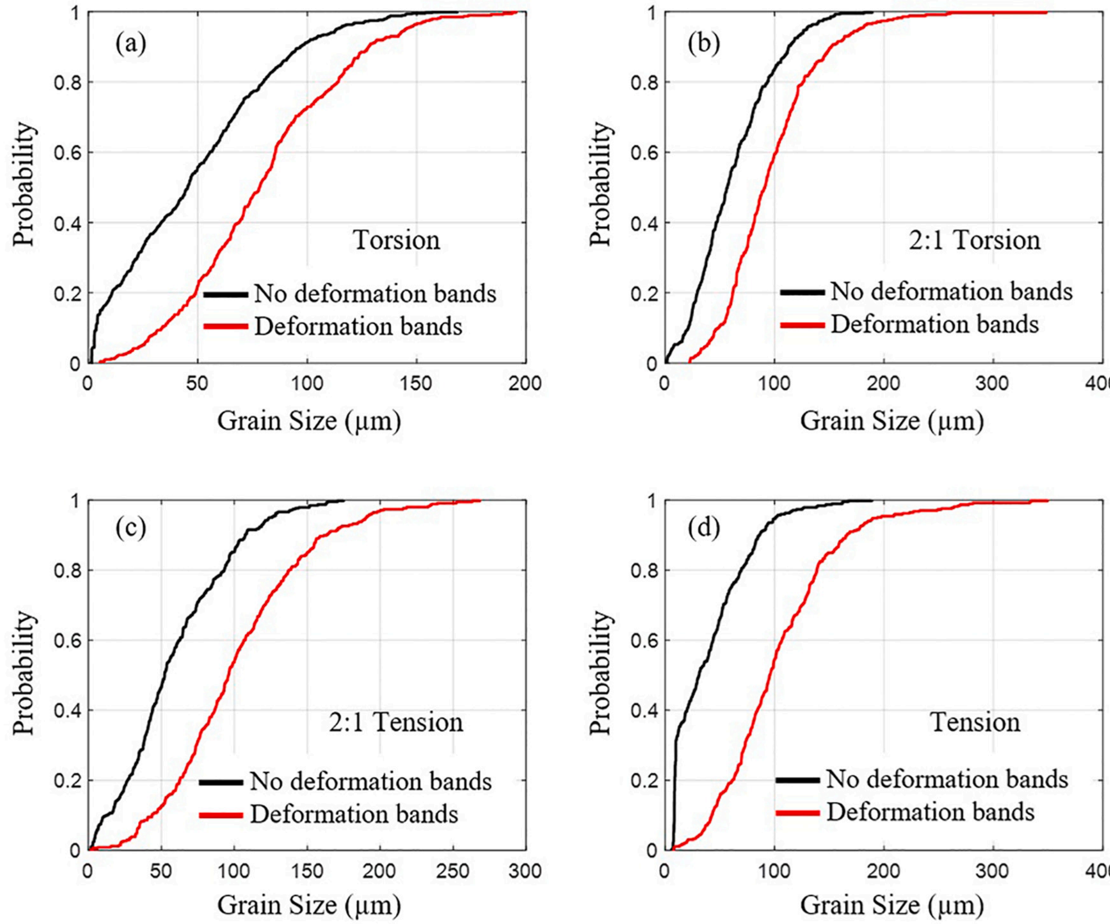

Fig. 12. The cumulative probability that DBs exist within grains as a function of size, as shown for the (a) torsion, (b) 2:1 torsion, (c) 2:1 tension and (d) tension specimens.

between each DB pixel and every surrounding GB pixel, the minimum distance was identified for each corresponding DB pixel. If the DB was coincident with the GB, the distance reported is zero. For the lowest percolation strain, 0.003, the DBD spans from 0° – 90°, as shown in Fig. 10(a), (d), (g) and (j). As the percolation strain increases to 0.006 and 0.009 the DBD trends toward 0°, as shown in Fig. 10(b-c), (e-f), (h-i) and (k-l). These results demonstrate that DBs have a greater effect on the pathways of DBs at relatively low strain magnitudes, while DBs with larger degrees of strain are more directly influenced by the plane of MSS.

For validity, the method utilized to determine the DB pathways should validate previous literature, wherein GBs are observed to accumulate the largest degree of deformation. The γ^{max} magnitudes were binned by distance to the nearest GB and are shown for each specimen within Fig. 11. As expected, DB locations near GBs localized the greatest degree of deformation and serve as a confirmation that the method utilized to define DBs is reasonable.

3.3. The role of grain size and texture on the pathway of deformation bands

The probability of a DB interacting with a grain based on the grain size (diameter) is examined for all loading cases. Utilizing the skeletonized DBs and a percolation strain of 0.003, grains with and without DBs were partitioned into two categories. For all specimens, the largest grains had the highest probability of containing a DB, as shown in Fig. 12. On average, DBs formed in grains whose diameter were 1.6 times larger, than grains without DBs.

The preference for DBs to form in a specific crystallographic orientation, relative to the plane of MSS, was examined for all grains within each specimen. For each specimen, the grain orientations were rotated by the angular difference between the specimen's longitudinal axis and the specimen's plane of MSS (about an axis normal to the plane of polish). An inverse pole figure projected onto the plane of MSS was created for each specimen, where grains with and without DBs are represented for a percolation strain of 0.003, as shown in Fig. 13. No clustering toward a given crystallographic orientation was observed within the inverse pole figures, indicating no strong preference for DBs to form within a specific grain orientation, relative to the plane of MSS. The same analysis was repeated for the larger percolation strains, 0.006 and 0.009, and for all percolation strains utilizing an inverse pole figure projection along the specimen's longitudinal axis, no preferred crystallographic orientation was observed for DB formation. The absence of a preferred grain orientation for DB formation is not surprising due to the weak fiber texture of the material.

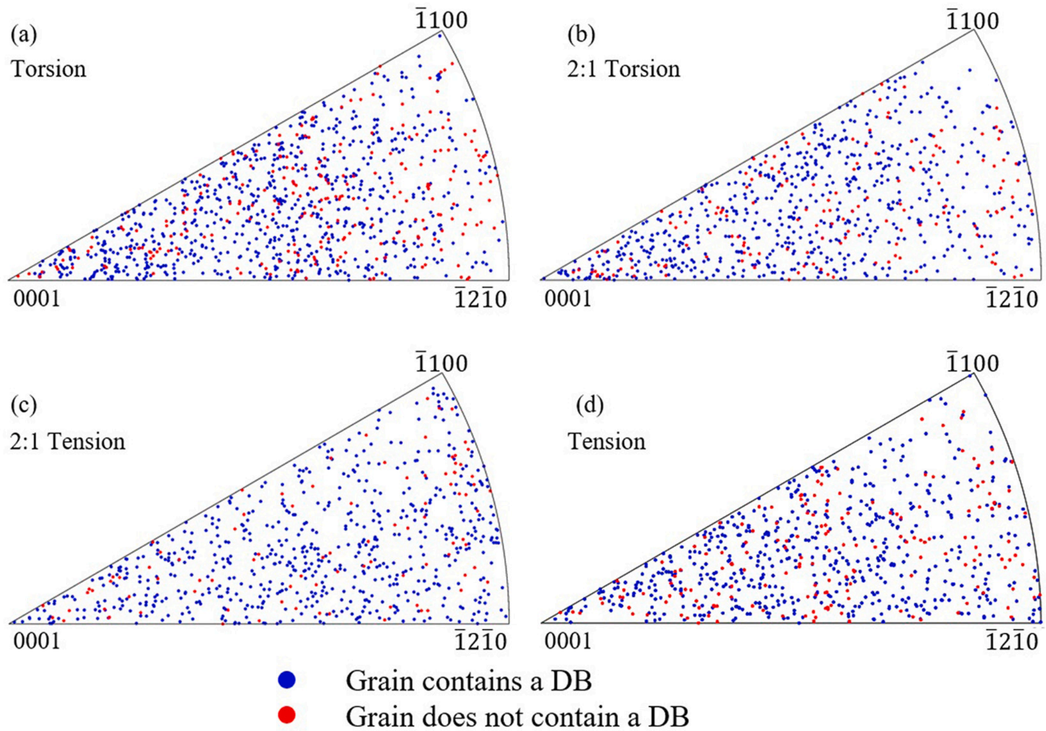

Fig. 13. Inverse pole figure projection of every grain with respect to the plane of MSS within the (a) torsion, (b) 2:1 torsion, (c) 2:1 tension and (d) tension specimens. Grains that contain a DB are shown in blue, while grains that do not contain DBs are shown in red. (For interpretation of the references to color in this figure legend, the reader is referred to the web version of this article.)

3.4. RVE sizing considering the residual deformation state and deformation band features

The methodologies presented in Section 2.5 established a relationship between the macroscopic strain state of the material, the macroscopic approach, and the number of DBs required to achieve an equivalent deformation state within a RVE, the micromechanical approach. The $\tilde{r}$ for each specimen is shown within Fig. 14a. At RVE edge lengths above 1000 μm the $\tilde{r}$ for all specimens are observed to converge, and above 1500 μm, the difference between individual specimens becomes negligible. The $\tilde{r}_{\varnothing}$ of all specimens is shown in Fig. 14b. A RVE edge length of 1610 μm minimizes $\tilde{r}_{\varnothing}$ and would encompass 446 grains of average diameter, 86 μm. The number of DBs that would appear in a RVE with an edge length of 1610 μm is calculated utilizing the mean DB measurements from Fig. 7 and Eq. 7. Approximately 18 DBs are required for the full range of percolation strains investigated as notated in Fig. 14b.

4. Discussion

The macroscopic tension torsion stress states resulted in plastic flow that formed DBs, which spanned multiple grains, as shown in Figs. 3 and 4. The presence of distinct deformation pathways through the microstructure were explicitly shown by Abuzaid et al. [10]. From such studies of uniaxial loading utilizing DIC, deformation bands are well aligned with the plane of MSS, yet from this single condition, the role of the microstructure was not able to be distinguished from the overall applied loading condition. In this study, the development of the DBs was assessed in relation to (i) the plane of MSS and (ii) microstructural features. Additionally, a mesoscale RVE edge length was determined which captured the variability in the mechanical response of the experiments as well as the DB features.

The DBs with the longest lengths and having the largest strains were found to be nearly coincident with the plane of MSS as determined by a Mohr's circle analysis for each loading condition. The distinct orientation and magnitude of DBs within the microstructure has been referred to as strain patterning. Utilizing DIC with slip band resolution, Lunt et al. [20] quantified the spatial strain variation based on strain patterning features, but did not address how the strain pattern was affected by the presence of GBs. In addition to agreeing with the continuum solution, the DBs identified utilizing the largest percolation strain, 0.009, were found to be the least perturbed by GBs, as shown in Fig. 10. In a way these DBs act as a conduit though which the largest deformations are accommodated. Past studies have shown that deformation which is inter-connected over two or more grains results in higher slip intensities along slip bands [47], promotes crack initiation [14], and are ultimately locations of material failure [13,48]. These results are consistent with the previous literature regarding slip inter-connectivity.

In tandem with DBs parallel to the plane of MSS, DBs of smaller length and having lower amounts of strain formed at orientations that differed from the plane of MSS to maintain compatibility within each specimen. This behavior is shown in Fig. 8, where portions of DBs can be seen deviating nearly perpendicular to the plane of MSS. Previous studies discuss the importance of compatibility between grains, wherein deformation of one grain requires the neighboring grains to also accommodate deformation, such that the interface between the grains remains intact [49–51]. This constraint creates stresses within the neighboring grain [11,52] and may cause deformation to occur in a

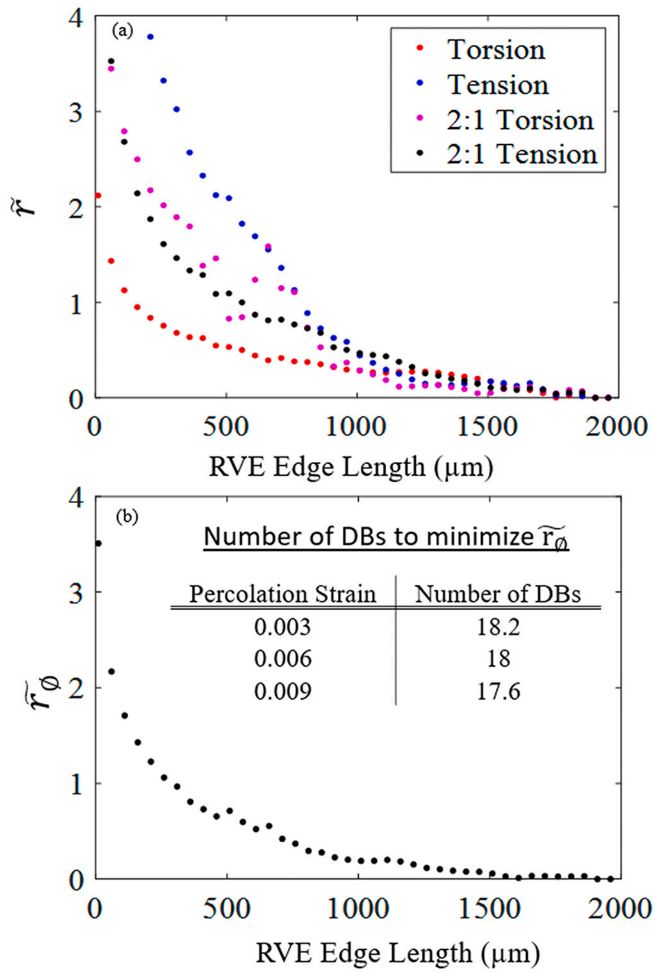

Fig. 14. (a) The average macroscopic error, $\tilde{r}$, and (b) the overall mechanical error, $\tilde{r}_{\varnothing}$, are shown as a function of the RVE edge length. The number of DBs, which minimize $\tilde{r}_{\varnothing}$ are noted for each percolation strain.

direction that does not coincide with the plane of MSS. Further, high energy x-ray diffraction microscopy (HEDM) experiments show that in the presence of a macroscopic uniaxial stress the grain level stresses produced are often similar in magnitude but occur in the all directions, including the directions normal to the applied load [53]. Utilizing HEDM, Chatterjee et al. [54] observed large variations in stress triaxiality within neighboring grains in Ti-7Al, positioning GBs as preferred sites for deformation deviation.

The largest deviation of DBs from the plane of MSS were found to coincide with GBs, wherein a DB would deviate along a GB. The stress near GBs is greater due to the obstruction of dislocation motion [12] and the aforementioned compatibility related stresses. In this study, the DBs with the lowest percolation strain, 0.003, experienced the largest deviations near GBs as compared to the larger percolation strain DBs, as shown in Fig. 10. This is in agreement with the theory of multi-slip [55,56] wherein the number of slip systems activated is governed by the amount of deformation accommodated, therefore larger percolation strain DBs have less deflection because of the increased slip system actively near the GB region. This finding is in concurrence with Ashby [30], wherein the effect of internal grain level stresses on deformation were most impactful before the onset of larger strain events such as multi-slip, which relieve the internal stresses near the GBs.

RVE sizing for Ti-7Al has been approached through a variety of characterization-based and simulation-based methodologies, which has in turn produced a range of effective RVE sizes, as shown in Table 4. The methodology of Balzani et al. [36] was modified in this study to apply the residual plastic strain to establish a RVE edge length. The novel aspects of the presented method are that the plastic strains measured through DIC are coupled to the global residual strain and that the required number of DBs for the RVE are determined. The reported RVE encompasses 446 grains and contain 18 DBs. The number of grains required in the presented RVE fall in the middle of Ti-7Al RVE investigations from the literature, which required between 200 grains and 750 grains, as shown in Table 4. The number of grains within the RVE presented in this study (446 grains) is 10% and 15% lower than the mean (493 grains) and median (515 grains) number of grain presented in literature-based Ti-7Al RVEs [32,35,57,58], respectively. A subset of the RVEs from the Ti-7Al literature are presented in Table 4. The presented RVE required fewer grains than many of the past Ti-7Al RVE investigations, this could be partially due to image resolution. As image magnification is increased, greater degrees of strain heterogeneities become visible [34]. This added variability will increase the number of grains needed within the RVE. Ti-7Al is a model material for more complex α/β titanium alloys, such as Ti-6242S (Ti-6Al-2Sn-4Zr-2Mo-0.1S by wt%) and Ti-6242 (Ti-6Al-2Sn-4Zr-2Mo by wt%). RVEs which have been utilized to instantiate crystal plasticity finite element simulations were selected from literature to compare with the current study [59–62], a subset of which is shown in Table 4. The number of grains within the RVE presented in this study (446 grains) is 9% and 5% higher than the mean (408 grains) and median (423 grains) number of grains presented in the Ti-6242S and Ti-6242 RVEs from literature [59–62], respectively. The number of grains required to capture the DB statistics and macroscopic deformation behavior is also in agreement with stereological observations which found the number of grains required to capture the mean grain size of a material is 500 grains [63]. Although the number of grains is similar when comparing the presented RVE and literature based RVEs the DB features tracked in this study are not readily visible in the literature RVEs. This difference is due to the surface area disparities which can be represented as a number of grains per edge length of the RVE. Comparatively, the RVE presented in this study requires, on average, between 1.6 and 2.5 times more grains per edge length, 18.7 grains per edge length, as compared to the Ti-6242(S) (11.9 grains per edge length) and Ti-7Al (7.3 grains per edge length) literature values, respectively. Increasing the number of grains per edge length of future simulations may increase the likelihood of capturing these interconnected DBs. Overall, the presented RVE methodology requires that the number of grains per edge length be increased to capture the mesoscale DB features investigated in this study. The meso-scale RVE methodology or MPSS model described within this study is widely applicable and can be utilized with any feature of interest and the resulting in-plane strain information.

The limitations of single camera DIC and optical image resolution are acknowledged as potential sources of uncertainty in the current study. More specifically, a single camera approach does not capture any out-of-plane displacement data. While every effort was made to keep the specimen surface planar, some deformation details could have been unmeasured due to this constraint. It should be noted that the crystallographic slip events were not captured as discrete events as shown in many high-resolution DIC studies, instead they were homogenized due to the resolution limitations of optical microscopy. The presented RVE edge length was 80% of the AOI edge length in each specimen. Each AOI contained 690 grains of average size. Future studies should consider imaging larger AOI's, containing 1000+ grains of average size to ensure that sufficient area is available for analysis. Lastly, the size of the DBs

Table 4
List of previous RVE investigations of Ti-7Al, Ti-6242 and Ti-6242S. Ti-7Al studies are ordered from largest to smallest number of grains per edge length. The method for determination and notes from each experiment are listed. The current study is highlighted.

Author	Material	Method for determination	Number of grains within RVE	Average grain size (μm)	Grains per edge length	Notes
Rotella, 2021	Ti7Al	See Sections 2.5 and 3.4	446	86	18.7	Current study
Ghosh, 2016 [58]	Ti7Al	2D EBSD characterization match of grain size and misorientation distributions	515, 529	40, 70	7.5, 13.7	Error metric minimized below 2% for RVEs containing more than 480 grains
Sangid, 2020 [35]	Ti7Al	Utilizing 3D HEDM measurements. Average or standard deviation of the sampled grains within 5% of the expected value.	200, 750	86	4.7, 7.3	The variability in the assessed quantities increases as a function of load. RVEs were evaluated at maximum load.
Ozturk, 2019 [32]	Ti7Al	2D EBSD characterization match of grain size and misorientation distributions	541	100	6.6	Micro-model used to evaluate regions of high stress in the macroscopic model.
Anahid, 2013 [59]	Ti-6242	2D EBSD characterization match of grain size and misorientation distributions	343	7.5, 15, 30	11.3	Stress fields from macroscopic FE models, micro-model informs trends in crack initiation
Zhang, 2020 [60]	Ti-6242S	2D EBSD characterization match of grain size and misorientation distributions	145	10.21	8.5	94% α-phase, small micro-model used to inform eigen deformation-based reduced-order model.

described here were measured under quasi-static loading conditions at room temperature. It should be noted that previous work by Follansbee and Gray [64] demonstrated higher strain rates or temperatures increase the number of active deformation mechanisms, such as twinning and cross-slip, within the alpha phase of titanium alloys. This may cause the DBs and the corresponding RVE edge length to vary in size.

5. Conclusions

A series of multiaxial deformation experiments were conducted on a near-alpha titanium alloy, wherein DB formation was examined over the mesoscale. A three-step process of strain thresholding, data percolation, and skeletonization defined the location DBs, which spanned many grains. The DBs overall orientation as well as any local angular deviations were assessed for all loading conditions and percolation strains. The DB statistics were utilized to explore the number of DBs needed to minimize the overall mechanical error of a RVE and were compared with RVE values from literature. The following conclusions can be derived from this study:

- The DBs which formed parallel to the plane of maximum shear stress, as determined by the Mohr's circle approach, were observed to be the longest and carried the largest degree of deformation. The spatial distribution of DBs is influenced by grain size, as they form in grains that are, on average, 1.6 times larger than the average grain size. The DBs did not prefer to form in grains with any specific crystallographic orientation.
- In tandem with the DBs formed parallel to the plane of maximum shear stress, smaller DBs, in both length and degree of deformation, formed an interconnected network to maintain compatibility in the specimens. These inter-connected DBs were more susceptible to deviations from the plane of maximum shear stress and occurred near GBs. The largest strain accumulations within the DBs were observed to occur near GBs.
- The mesoscale plastic strain sizing (MPSS) model utilized DB features and in-plane-plastic strain measurements to establish a RVE edge length. Both the macroscopic residual deformation and underlying DBs were used in tandem to describe a mesoscopic RVE edge length that could capture the overall deformation response as well as the

population of the DBs within the RVE. The overall mechanical error is minimized when the RVE edge length is 1610 μm, which encompasses an average of 446 grains and 18 DBs for all three percolation strains. As the RVE becomes smaller the mechanical response no longer matches the global response of the specimen, due to an exponential increase in the overall mechanical error. In order to capture well defined DB features within an RVE, this 2D analysis recommends 18.7 grains per RVE edge length which is significantly more than previous studies in the literature utilizing similar material, as referenced in Table 4.

Data availability

The processed data required to reproduce these findings (in terms of the DIC strains, EBSD data, and percolated strain paths) are available to download from the following URL: https://data.mendeley.com/datasets/rrgpxcknf5/2

Declaration of Competing Interest

The authors declare that they have no known competing financial interests or personal relationships that could have appeared to influence the work reported in this paper.

Acknowledgments

Financial support for the deformation pathway experiment was provided by the Air Force Research Lab, Materials and Manufacturing Directorate. MDS acknowledges support from the National Science Foundation (grant number CMMI 16–51956). Partial support for J.R. was provided by the Department of Defense through the National Defense Science and Engineering Graduate Fellowship Program (NDSEG). Dr. Ayman Salem is acknowledged for helpful conversations on the electropolishing of titanium and higher order statistics. Dr. Andy Rosenberger and Phil Blosser are acknowledged for helpful conversations regarding multiaxial loading experiments.

References

[1] M. Hatherly, A.S. Malin, Shear bands in deformed metal, Scr. Metall. 18 (1984) 449–454.
[2] M.D. Sangid, The physics of fatigue crack initiation, Int. J. Fatigue 57 (2013) 58–72, https://doi.org/10.1016/j.ijfatigue.2012.10.009.
[3] M.D. Sangid, T. Ezaz, H. Sehitoglu, Energetics of residual dislocations associated with slip-twin and slip-GBs interactions, Mater. Sci. Eng. A 542 (2012) 21–30, https://doi.org/10.1016/j.msea.2012.02.023.
[4] I.L. Dillamore, J.G. Roberts, A.C. Bush, Occurrence of shear bands in heavily rolled cubic metals, Met. Sci. 13 (1979) 73–77, https://doi.org/10.1179/msc.1979.13.2.73.
[5] G.E. Dieter, Mechanical Metallurgy, 615 p, http://catalog.hathitrust.org/Record/000592040, 1961.
[6] K. Morii, Y. Nakayama, Shear bands in rolled copper single crystals, Trans. Jpn. Inst. Met. 22 (1981) 857–864.
[7] Y. Nakayama, K. Morii, Transmission Formation Electron Microscopy of Shear Band in Rolled Copper Single Crystals, 1982, pp. 422–431.
[8] H.E. Dève, R.J. Asaro, The development of plastic failure modes in crystalline materials: shear bands in Fcc polycrystals, Metall. Trans. A. 20 (1989) 579–593, https://doi.org/10.1007/BF02667576.
[9] A. Korbel, J.D. Embury, M. Hatherly, P.L. Martin, H.W. Erbsloh, Aspects of strain in Al-Mg alloys, Acta Metall. 34 (1986) 1999–2009.
[10] W.Z. Abuzaid, M.D. Sangid, J.D. Carroll, H. Sehitoglu, J. Lambros, Slip transfer and plastic strain accumulation across grain boundaries in Hastelloy X, J. Mech. Phys. Solids. 60 (2012) 1201–1220, https://doi.org/10.1016/j.jmps.2012.02.001.
[11] J.P. Hirth, The influence of grain boundaries on mechanical properties, Metall. Trans. A. 3 (1972) 3047–3067.
[12] A.N. Stroh, The formation of cracks as a result of plastic flow, Proc. R. Soc. A Math. Phys. Eng. Sci. 223 (1954) 404–414, https://doi.org/10.1098/rspa.1954.0124.
[13] D.L. Davidson, R.G. Tryon, M. Oja, R. Matthews, K.S. Ravi Chandran, Fatigue crack initiation in WASPALOY at 20 °C, Metall. Mater. Trans. A. 38 (2007) 2214–2225, https://doi.org/10.1007/s11661-007-9178-6.
[14] M.D. Sangid, H.J. Maier, H. Sehitoglu, The role of grain boundaries on fatigue crack initiation – an energy approach, Int. J. Plast. 27 (2011) 801–821, https://doi.org/10.1016/j.ijplas.2010.09.009.
[15] W.H. Peters, W.F. Ranson, M.A. Sutton, T.C. Chu, J. Anderson, Application of digital correlation methods to rigid body mechanics, Opt. Eng. 22 (1983) 738–742.
[16] S. Sandlöbes, I. Schestakow, S. Yi, S. Zaefferer, J. Chen, M. Friák, J. Neugebauer, D. Raabe, The relation between shear banding, microstructure and mechanical properties in mg and mg-Y alloys, Mater. Sci. Forum 690 (2011) 202–205, https://doi.org/10.4028/www.scientific.net/MSF.690.202.
[17] T.C. Chu, W.F. Ranson, M.A. Sutton, W.H. Peters, Applications of digital image correlation techniques to experimental mechanics, Exp. Mech. 25 (1985) 232–244, https://doi.org/10.1007/BF02325092.
[18] Y.L. Dong, B. Pan, A review of speckle pattern fabrication and assessment for digital image correlation, Exp. Mech. 57 (2017) 1161–1181, https://doi.org/10.1007/s11340-017-0283-1.
[19] M.D. Sangid, T.A. Book, D. Naragani, J. Rotella, P. Ravi, A. Finch, P. Kenesei, J. Park, H. Sharma, J. Almer, Role of heat treatment and build orientation in the microstructure sensitive deformation characteristics of IN718 produced via SLM additive manufacturing, Addit. Manuf. 22 (2018) 479–496, https://doi.org/10.1016/j.addma.2018.04.032.
[20] D. Lunt, A. Orozco-Caballero, R. Thomas, P. Honniball, P. Frankel, M. Preuss, J. Quinta da Fonseca, Enabling high resolution strain mapping in zirconium alloys, Mater. Charact. 139 (2018) 355–363, https://doi.org/10.1016/j.matchar.2018.03.014.
[21] E.O. Hall, The deformation and ageing of mild steel: III discussion of results, Proc. Phys. Soc. Sect. B. 64 (1951) 747–753, https://doi.org/10.1088/0370-1301/64/9/303.
[22] N.J. Petch, The cleavage strength of polycrystals, J. Iron Steel Inst. 174 (1953).
[23] B.S. Fromm, B.L. Adams, S. Ahmadi, M. Knezevic, Grain size and orientation distributions: application to yielding of α-titanium, Acta Mater. 57 (2009) 2339–2348, https://doi.org/10.1016/j.actamat.2008.12.037.
[24] D. Lunt, A. Ho, A. Davis, A. Harte, F. Martina, J. Quinta da Fonseca, P. Prangnell, The effect of loading direction on strain localisation in wire arc additively manufactured Ti–6Al–4V, Mater. Sci. Eng. A 788 (2020), https://doi.org/10.1016/j.msea.2020.139608.
[25] L. Bodelot, Investigation of the relationship between microstructural features and strain localization in polycrystalline 316 L, Exp. Mech. 59 (2019) 691–702, https://doi.org/10.1007/s11340-019-00508-0.
[26] M.R. Bache, W.J. Evans, B. Suddell, F.R.M. Herrouin, The effects of texture in titanium alloys for engineering components under fatigue, Int. J. Fatigue 23 (2001) 153–159, https://doi.org/10.1016/s0142-1123(01)00124-4.
[27] T.A. Book, M.D. Sangid, Strain localization in Ti-6Al-4V Widmanstätten microstructures produced by additive manufacturing, Mater. Charact. 122 (2016) 104–112, https://doi.org/10.1016/j.matchar.2016.10.018.
[28] M.E. Harr, S. Daly, A.L. Pilchak, The effect of temperature on slip in microtextured Ti-6Al-2Sn-4Zr-2Mo under dwell fatigue, Int. J. Fatigue 147 (2021) 106173, https://doi.org/10.1016/j.ijfatigue.2021.106173.
[29] W.J. Evans, J.P. Jones, M.T. Whittaker, Texture effects under tension and torsion loading conditions in titanium alloys, Int. J. Fatigue 27 (2005) 1244–1250, https://doi.org/10.1016/j.ijfatigue.2005.06.045.
[30] M.F. Ashby, The deformation of plastically non-homogeneous materials, Philos. Mag. 21 (1970) 399–424, https://doi.org/10.1080/14786437008238426.
[31] R. Hill, Elastic properties of reinforced solids: some theoretical principles, J. Mech. Phys. Solids. 11 (1963) 357–372, https://doi.org/10.1016/0022-5096(63)90036-X.
[32] D. Ozturk, S. Kotha, A.L. Pilchak, S. Ghosh, Two-way multi-scaling for predicting fatigue crack nucleation in titanium alloys using parametrically homogenized constitutive models, J. Mech. Phys. Solids. 128 (2019) 181–207, https://doi.org/10.1016/j.jmps.2019.04.009.
[33] S.R. Yeratapally, M.G. Glavicic, M. Hardy, M.D. Sangid, Acta Materialia microstructure based fatigue life prediction framework for polycrystalline nickel-base superalloys with emphasis on the role played by twin boundaries in crack initiation, Acta Mater. 107 (2016) 152–167, https://doi.org/10.1016/j.actamat.2016.01.038.
[34] C. Efstathiou, H. Sehitoglu, J. Lambros, Multiscale strain measurements of plastically deforming polycrystalline titanium: role of deformation heterogeneities, Int. J. Plast. 26 (2010) 93–106, https://doi.org/10.1016/j.ijplas.2009.04.006.
[35] M.D. Sangid, J. Rotella, D. Naragani, J.-S. Park, P. Kenesei, P.A. Shade, A complete grain-level assessment of the stress-strain evolution and associated deformation response in polycrystalline alloys, Acta Mater. 201 (2020) 36–54, https://doi.org/10.1016/j.actamat.2020.09.051.
[36] D. Balzani, L. Scheunemann, D. Brands, J. Schröder, Construction of two- and three-dimensional statistically similar RVEs for coupled micro-macro simulations, Comput. Mech. 54 (2014) 1269–1284, https://doi.org/10.1007/s00466-014-1057-6.
[37] A.L. Pilchak, J. Li, S.I. Rokhlin, Quantitative comparison of microtexture in near-alpha titanium measured by ultrasonic scattering and electron backscatter

diffraction, Metall. Mater. Trans. A Phys. Metall. Mater. Sci. 45 (2014) 4679–4697, https://doi.org/10.1007/s11661-014-2367-1.
[38] M.G. Glavicic, T. Morton, T. Broderick, V. Venkatesh, F. Zhang, D. Boyce, W. Wu, A.A. Salem, I. Dempster, V. Saraf, Y. Kosaka, A. Pilchak, C. Woodward, S. L. Semiatin, Progress in the advanced titanium microstructure and modeling program, in: Proc. 13th World Conf. Titan, 2016, pp. 1863–1873, https://doi.org/10.1002/9781119296126.ch312.
[39] D. Ozturk, A.L. Pilchak, S. Ghosh, Experimentally validated dwell and cyclic fatigue crack nucleation model for α–titanium alloys, Scr. Mater. 127 (2017) 15–18, https://doi.org/10.1016/j.scriptamat.2016.08.031.
[40] J. Tracy, A. Waas, S. Daly, A new experimental approach for in situ damage assessment in fibrous ceramic matrix composites at high temperature, J. Am. Ceram. Soc. 98 (2015) 1898–1906, https://doi.org/10.1111/jace.13538.
[41] F. Di Gioacchino, J. Quinta Da Fonseca, An experimental study of the polycrystalline plasticity of austenitic stainless steel, Int. J. Plast. 74 (2015) 92–109, https://doi.org/10.1016/j.ijplas.2015.05.012.
[42] T.R. McNelley, D.L. Swisher, M.T. Prez-Prado, Deformation bands and the formation of grain boundaries in a superplastic aluminum alloy, Metall. Mater. Trans. A Phys. Metall. Mater. Sci. 33 (2002) 279–290, https://doi.org/10.1007/s11661-002-0089-2.
[43] D. Arora, I. Cooper, An Introduction to Percolation Theory A Matlab Simulation, Github. https://d-arora.github.io/Doing-Physics-With-Matlab/mpDocs/percolation.htm. (Accessed 8 July 2021) (n.d.).
[44] S.R. Niezgoda, D.M. Turner, D.T. Fullwood, S.R. Kalidindi, Optimized structure based representative volume element sets reflecting the ensemble-averaged 2-point statistics, Acta Mater. 58 (2010) 4432–4445, https://doi.org/10.1016/j.actamat.2010.04.041.
[45] D.T. Fullwood, S.R. Kalidindi, S.R. Niezgoda, A. Fast, N. Hampson, Gradient-based microstructure reconstructions from distributions using fast Fourier transforms, Mater. Sci. Eng. A 494 (2008) 68–72, https://doi.org/10.1016/j.msea.2007.10.087.
[46] C.A. Schneider, W.S. Rasband, K.W. Eliceiri, NIH image to ImageJ: 25 years of image analysis, Nat. Methods 9 (2012) 671–675, https://doi.org/10.1038/nmeth.2089.
[47] J. Rotella, M.D. Sangid, Microstructural-based strain accumulation during cyclic loading of Ni-based superalloys: the role of neighboring grains on interconnected slip bands, Fatigue Fract. Eng. Mater. Struct. 43 (2020) 2270–2286, https://doi.org/10.1111/ffe.13257.
[48] W. Abuzaid, H. Sehitoglu, J. Lambros, Plastic strain localization and fatigue micro-crack formation in Hastelloy X, Mater. Sci. Eng. A 561 (2012) 507–519, https://doi.org/10.1016/j.msea.2012.10.072.
[49] G.I. Taylor, Plastic strain in metals, J. Inst. Met. 62 (1938) 307–325.
[50] C. Blochwitz, W. Tirschler, Twin boundaries as crack nucleation sites, Cryst. Res. Technol. 40 (2005) 32–41, https://doi.org/10.1002/crat.200410305.
[51] J.P. Hirth, The influence of grain boundaries on mechanical properties, Chem. Phys. Met. Comm. AIME. 3 (1957) 1955–1957. https://link.springer.com/content/pdf/10.1007%2FBF02661312.pdf.
[52] J. Miao, T.M. Pollock, J. Wayne Jones, Crystallographic fatigue crack initiation in nickel-based superalloy René 88DT at elevated temperature, Acta Mater. 57 (2009) 5964–5974, https://doi.org/10.1016/j.actamat.2009.08.022.
[53] J.C. Schuren, P.A. Shade, J.V. Bernier, S. Fai, B. Blank, J. Lind, P. Kenesei, U. Lienert, R.M. Suter, T.J. Turner, D.M. Dimiduk, J. Almer, New opportunities for quantitative tracking of polycrystal responses in three dimensions, Curr. Opin. Solid State Mater. Sci. 19 (2015) 235–244, https://doi.org/10.1016/j.cossms.2014.11.003.
[54] K. Chatterjee, A. Venkataraman, T. Garbaciak, J. Rotella, M.D. Sangid, A. J. Beaudoin, P. Kenesei, J.S. Park, A.L. Pilchak, Study of grain-level deformation and residual stresses in Ti-7Al under combined bending and tension using high energy diffraction microscopy (HEDM), Int. J. Solids Struct. 94–95 (2016) 35–49, https://doi.org/10.1016/j.ijsolstr.2016.05.010.
[55] J.D. Livingston, B. Chalmers, Multiple slip in bicrystal deformation, Acta Metall. 5 (1957) 322–327, https://doi.org/10.1016/0001-6160(57)90044-5.
[56] J.J. Hauser, B. Chalmers, The plastic deformation of bicrystals of f.c.c. metals, Acta Metall. 9 (1961) 802–818, https://doi.org/10.1016/0001-6160(61)90183-3.
[57] T. Maloth, D. Ozturk, G.M. Hommer, A.L. Pilchak, A.P. Stebner, S. Ghosh, Multiscale modeling of cruciform dwell tests with the uncertainty-quantified parametrically homogenized constitutive model, Acta Mater. 200 (2020) 893–907, https://doi.org/10.1016/j.actamat.2020.09.037.
[58] S. Ghosh, A. Shahba, X. Tu, E.L. Huskins, B.E. Schuster, Crystal plasticity FE modeling of Ti alloys for a range of strain-rates. Part II: Image-based model with experimental validation, Int. J. Plast. 87 (2016) 69–85, https://doi.org/10.1016/j.ijplas.2016.09.003.
[59] M. Anahid, S. Ghosh, Homogenized constitutive and fatigue nucleation models from crystal plasticity FE simulations of Ti alloys, part 2: macroscopic probabilistic crack nucleation model, Int. J. Plast. 48 (2013) 111–124, https://doi.org/10.1016/j.ijplas.2013.02.008.
[60] Y. Liu, X. Zhang, Y. Zhu, P. Hu, Dislocation Density Informed Eigenstrain Based Reduced Order Homogenization Modeling : Verification and Application on a Titanium Alloy Structure Subjected to Cyclic Loading Dislocation Density Informed Eigenstrain Based Reduced Order Homogenization Model, 2020.
[61] S. Kotha, D. Ozturk, S. Ghosh, Parametrically homogenized constitutive models (PHCMs) from micromechanical crystal plasticity FE simulations, part I: sensitivity analysis and parameter identification for titanium alloys, Int. J. Plast. 120 (2019) 296–319, https://doi.org/10.1016/j.ijplas.2019.05.008.
[62] D. Ozturk, Quantification of Deformation and Fatigue Crack Nucleation in Titanium Alloys Using, 2019.
[63] E.J. Payton, Revisiting sphere unfolding relationships for the stereological analysis of segmented digital microstructure images, J. Miner. Mater. Charact. Eng. 11 (2012) 221–242, https://doi.org/10.4236/jmmce.2012.113018.
[64] P.S. Follansbee, G.T. Gray, An analysis of the low temperature, low and high strain-rate deformation of Ti-6Al-4V, Metall. Trans. A. 20 (1989) 863–874, https://doi.org/10.1007/BF02651653.